


Multi-objective optimization of the process combining ultrasonic vibration and age-forming of dissimilar friction-stir-welded Aluminium T-stiffened plates

Duquan Zuo^{1,*} , Yanjie Han¹, Ti Ye¹, Tianyu Xu¹, Shilin Feng¹, Yuanxiu Zhang¹, Shaoqing Jin¹, and Sean Gao²

¹ Sichuan Province Engineering Technology Research Center of General Aircraft Maintenance, Civil Aviation Flight University of China, 46 Nanchang Road, Guanghan, 618307, PR China

² School of Engineering, University of Tokyo, 7-3-1 Hongo, Bunkyo-ku, Tokyo 113-8656, Japan

Received: 19 April 2025 / Accepted: 5 November 2025

Abstract. This paper innovatively proposes a combined process combining ultrasonic vibration (abbreviated UV) with creep age forming (abbreviated CAF), named UVCAF, for high-quality forming of dissimilar 7055-T6/2197-T8 FSWed T-stiffened plates. And based on this, a multi-objective optimization quality comprehensive evaluation model of the AMOGA-EWM algorithm is proposed, obtaining the optimal process parameter solution combination as [164.8 °C, 9.2h, 9.6 μm]. The reliability and feasibility of the above evaluation model in improving the forming rate and mechanical properties for the T-stiffened plates are verified. Meanwhile, through comparative analysis of the experimental results of UVCAF under the optimal process parameters, it is found that the forming rate, tensile strength, and elongation of T-stiffened plates under UVCAF are 5.4%, 12.3 MPa, and 0.82% higher than those under CAF. In addition, the microscopic analysis results indicate that the fracture mode of the specimens under CAF and UVCAF is a ductile fracture, and the weld nugget zone of the specimens under CAF and UVCAF is the combined reinforcement of the T₁ and η phase. However, the introduction of UV through the strengthening effect of fine grains makes the η phase more abundant in UVCAF specimens, thereby improving the forming accuracy and performance of the specimens.

Keywords: T-stiffened plates / FSW / ultrasonic vibration / creep aging forming / multi-objective optimization

1 Introduction

Friction stir welding (FSW), as an emerging solid-state joining technology [1], has broad prospects for applications in the connection of structural components such as aircraft skin panels, central wing boxes, and wings. However, Zuo et al. [2] found in the FSW-T joint welding process that the uneven heating of various regions of the T-joint can lead to a gradual decrease in temperature along the width of the weld nugget zone of the T-stiffened plate, resulting in complex structural changes and uneven distribution of residual stresses in the T-joint. Large integral panels of aircraft fuselages belong to the category of columnar panel forming, and CAF is one of the key technologies for the forming of such panels. CAF involves implementing creep and artificial aging simultaneously at a certain temperature to release as many residual stresses in the panel as possible, thereby achieving the forming and strengthening of the

integral stiffened plate [3]. Compared to traditional forming methods such as rolling and shot peening, CAF specimens exhibit characteristics such as low residual stresses and good forming performance [4,5], presenting broad prospects in the manufacturing of large integral panels [6], especially in the lightweight of dissimilar alloy welded large integral panels.

However, there is a significant springback in CAF specimens after unloading, which seriously affects their forming accuracy. The introduction of UV can effectively solve the above-mentioned issue by not only reducing and homogenizing residual stresses within the material but also decreasing forming forces and improving forming quality [7]. Yang, Li et al. [8,9] have used UV to reduce residual stresses inside abrasive diamonds and deformation stresses in entropy alloys, enhancing their plastic strain. Liu and colleagues [10] conducted ultrasonic vibration-assisted micro-tension tests on T₂ copper foil, analyzed the fracture morphology and revealed the microscopic mechanism of the acoustic softening effect. To prepare ultrafine-grained Al 6061 alloy strips, Pi et al. [11] proposed a new process of

* e-mail: taiyanghefeng@cafuc.edu.cn

Table 1. Chemical composition of Al 7055-T6 and Al-Li 2197-T8 alloys (mass fraction, %).

7055-T6 alloy	Zn	Mg	Cu	Zr	Fe	Mn	Si	Ti	Cr	Al
	7.9	2.1	2.3	0.05	0.15	0.05	0.1	0.06	0.001	Bal.
2197-T8 alloy	Li	Cu	Ag	Mn	Mg	Zr	Fe	Si	Zn	Al
	1.5	2.88	0.36	0.35	0.24	0.09	0.05	0.04	0.006	Bal.

Table 2. Room temperature properties of 7055-T6 and 2197-T8 alloys.

Materials	Transverse tensile strength / MPa	Longitudinal tensile strength / MPa	Elongation/ %	Melting point/ °C
7055-T6	600	540	13	590
2197-T8	570	530	6	560

axially ultrasonic vibration-assisted extrusion cutting, which resulted in better surface flatness and smoothness of chip samples compared to traditional cutting processes. For copper T₂ ultrasonic micro-extrusion experiments, Han et al. [12] designed a novel ultrasonic micro-extrusion process with a tool-workpiece composite vibration, finding that this process achieved better micro-extrusion forming characteristics. Furthermore, Zhou and colleagues [13] developed an ultrasonic vibration-assisted forming system and found that when the ultrasonic power reached 1.8 KW, it could reduce the yield stress of copper. Cao et al. [14] introduced an ultrasonic vibration plate device capable of achieving longitudinal full-wave and transverse half-wave (L₂T₁) vibration modes, which reduced the grinding force on Inconel 718 nickel-based superalloy and improved the surface quality. Currently, UV methods mainly focus on research on the same materials, and reports on dissimilar materials are rare. Additionally, Szpunar [15] used a central composite design method to construct a second-order quadratic model to determine the optimal input parameters for optimizing single-point incremental forming processes. Dillip et al. [16] established an optimization model based on multi-objective genetic algorithms (MOGA) to improve the forming rate in machining processes, reduce costs, and minimize product scrap. It can be observed that in any machining process, optimizing process quality through process parameter optimization methods [17] is another effective way to achieve the best and most efficient outputs.

Therefore, this paper innovatively proposes a composite forming method suitable for the UVCAF process of dissimilar FSWed T-stiffened plates. Firstly, a single-objective polynomial response surface model is constructed using the central composite design method (CCD), and the rationality of the model is analyzed using analysis of variance (ANOVA) and residual analysis methods. Secondly, an improved algorithm combining the adaptive multi-objective genetic algorithm (AMOGA) and the entropy weighting method (EWM), named AMOGA-EWM, is used to perform multi-objective optimization on the aforementioned single-objective model. Experimental verification is conducted on self-made UVCAF specialized equipment. Furthermore, a comparison of the macroscopic

and microscopic aspects of UVCAF and CAF experimental results is carried out to demonstrate the accuracy and reliability of the multi-objective optimization model. It provides a reference for the high-precision, high-performance integrated manufacturing of lightweight aircraft's large integral panels.

2 Materials and experimental methods

2.1 Specimens and forming device

In this experiment, pre-strained 7055-T6 [18] Al alloy was selected as the skin, with dimensions of 200 × 80 × 1.5 mm, and 2197-T8 Al-Li alloy was used as the stiffener, with dimensions of 200 × 5 × 13 mm. The chemical composition and room temperature properties of the alloys are shown in Tables 1 and 2. The large integral panel of the aircraft fuselage is mainly composed of skin and stiffeners (see Fig. 1a), with the FSWed T-stiffened plate equivalent to a single stiffener specimen cut along the X direction of the columnar panel (see Fig. 1b). Physical images are shown in Figures 1c and 1d. It should be emphasized that when the columnar panel is bent, the stiffeners aligned in the axial direction can be ignored [19].

The UVCAF experiment requires ensuring that the vibration waves are effectively transmitted to the T-stiffened plate inside the thermal environment in the form of longitudinal waves. Therefore, in this experiment, UV was introduced into the forming die directly below the tooling during CAF. The forming die was fixed and installed inside a temperature-controlled chamber with pillar 4, and mould 7 was connected to the external vibration source via special screw 6. The specialized fixture for fixing the vibration is illustrated in Figure 2a, and the vibration is shown in Figure 2b. The ultrasonic vibration device consists of a transducer, an amplifying bar, a vibration transmission bar, and a vibration fixture, as shown in the schematic in Figure 3a, with the forming device depicted in Figure 3b.

Due to the small amplitude generated by the transducer, a 20 kHz ultrasonic frequency can only produce a few microns of amplitude. To increase the mechanical vibration applied to the tooling, an ultrasonic amplitude

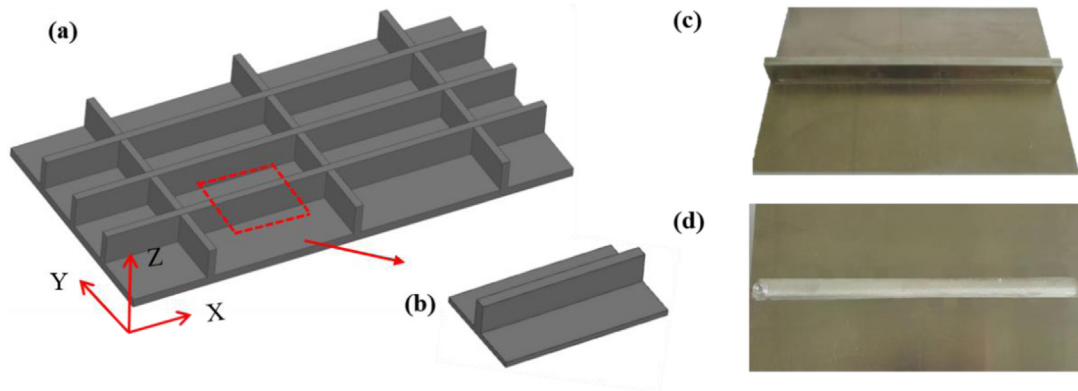
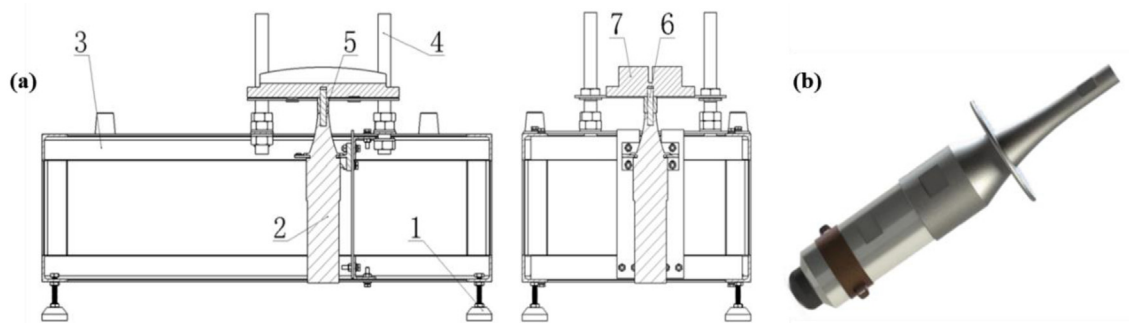


Fig. 1. Geometry of (a) integral panel and its Simplified (b) T-stiffened plate, and the views of (c) front and (d) back for the mentioned previously T-stiffened plate.



Note: 1 Adjustable foot pad, 2 Vibrator, 3 Vibration platform, 4 Pillar, 5 Vibration bar, 6 Special screw, 7 Mould

Fig. 2. Illustrations of the (a) fixed vibrator tooling and (b) vibrator.

adjuster is connected between the end face of the transducer and the vibration fixture to achieve the functions of energy focusing and impedance matching [20]. Therefore, this experiment utilizes a self-made three-stage composite amplifying bar with an exponential transition section to enhance the output performance, as shown in the structure and coordinate system in Figure 4.

The dimensions marked in the figure are: $l_1 = 27.6$ mm, $l_2 = 67.4$ mm, $l_3 = 27.6$ mm, $l = 122.6$ mm, $\Phi_1 = 60$ mm, $\Phi_2 = 10$ mm, $\Phi_3 = 82.1$ mm. It is worth emphasizing that the amplitude adjuster in the above figure is made of TC4 titanium alloy material, where section I and section III are rods with equal circular cross-sections, section II is a rod with an exponential variable circular cross-section, and sections I and II are integral in structure and connected to section III by a special screw.

2.2 Multi-objective optimization of process parameters

2.2.1 Modeling and analysis

During the UVCAF experiment, phenomena such as creep, stress superposition, ultrasonic softening, and work hardening are observed, with a significant impact of UV on the forming quality of the specimens. When subjected to high amplitude vibration, not only does it increase the

internal stress of the material, but it also reduces the material's softening effect, hinders its plastic flow ability, and consequently reduces its strength; prolonged vibration leads to deterioration of the viscoplasticity of the aged tensile specimens [21]. Therefore, only appropriate vibration energy can maximally release the residual stresses in the material, enhancing its viscoplastic forming capability. To improve the forming accuracy and performance of the T-stiffened plate, creep temperature x_1 , creep time x_2 , and amplitude x_3 were selected as design factors, while forming rate Y_1 , tensile strength Y_2 , and elongation Y_3 were set as optimization objectives. A multi-objective optimization method was employed to obtain the optimal combination of process parameters to enhance the forming rate and mechanical performance of the T-stiffened plates. Initially, the CCD method was used to construct a continuous variable response surface model [22,23], evaluate the impact factors of the objectives and their interactions, define the optimal level ranges, and design the UVCAF experimental results based on the CCD method, as shown in Table 3. It is noteworthy that for ease of calculation, the optimization objectives (Y_1 , Y_2 , and Y_3) were reciprocally transformed (Y_1' , Y_2' , and Y_3') to avoid errors caused by magnitude differences among the reciprocals of the objectives. The transformed Y_1' and Y_3' were magnified

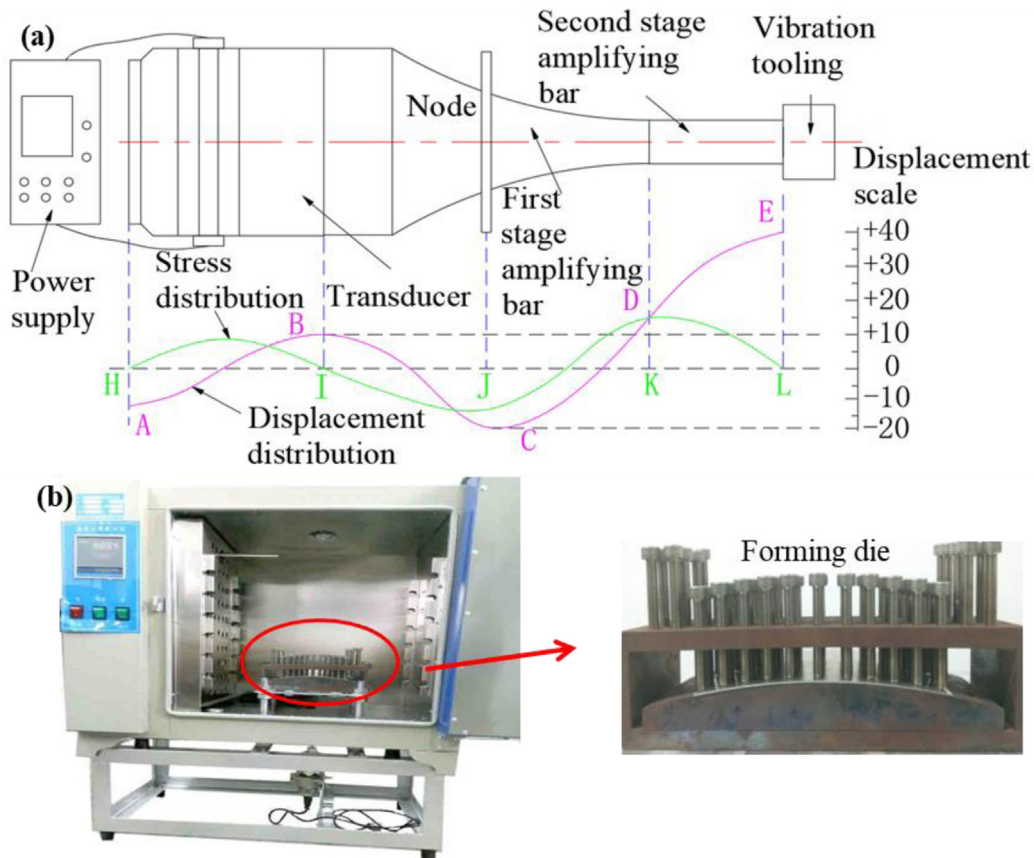


Fig. 3. Schematic of (a) ultrasonic wave transmission principle and views of (b) forming device.

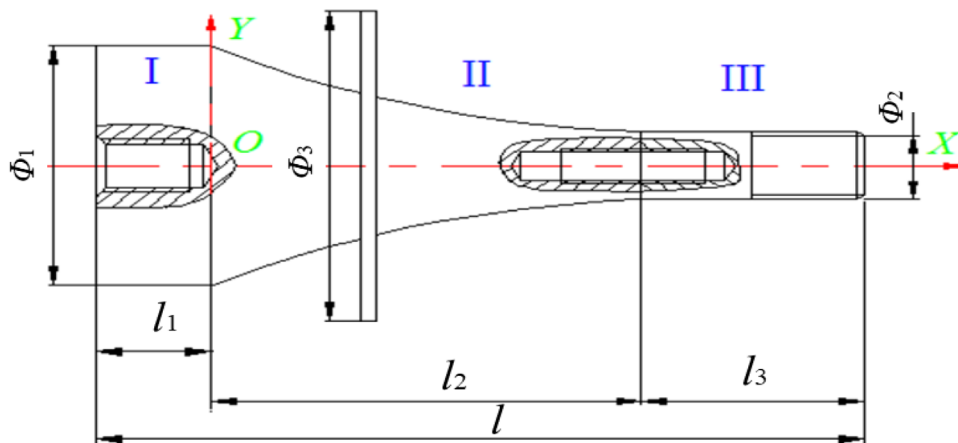


Fig. 4. Geometry of the amplifying bar.

by 10^4 times, while Y_2' was magnified by 10^6 times. Furthermore, a three-factor quadratic regression model was used to fit the optimized process parameters, resulting in a fitted second-order response surface model:

$$\bar{Y} = \bar{b}_0 + \sum_{i=1}^k \bar{b}_i x_i + \sum_{i < j} b_{ij} x_i x_j + \sum_{i=1}^k \bar{b}_{ii} x_i^2. \quad (1)$$

In the equation, $\bar{b}_0, \bar{b}_i, \bar{b}_{ij}, \bar{b}_{ii}$ are all constant terms. Let $x_i = x_i, x_i^2 = x_{i+k}, x_{k-1} \sim x_k = x_{k(k+1)/2}, \bar{b}_i = \bar{b}_i, \bar{b}_{ij} = \bar{b}_{i+k}, \bar{b}_{(k+1)k} = \bar{b}_{k(k+3)/2}, n = 0.5k(k+3)$, where i takes natural numbers from $\{1, 2, \dots, k\}$, then formula (1) can be simplified as:

$$\bar{Y} = \bar{b}_0 + n \sum_{i=1}^n \bar{b}_i x_i. \quad (2)$$

Table 3. Results of CCD experimental design.

No	Forming parameters			Experimental result		
	$x_1/^\circ\text{C}$	x_2/h	$x_3/\mu\text{m}$	Y_1'	Y_2'/MPa	Y_3'
1	140.000	6.0000	8.8600	150.105	2476.596	1375.516
2	185.000	6.0000	8.8600	126.247	2467.247	1342.282
3	140.000	12.0000	8.8600	134.825	2376.143	1277.139
4	185.000	12.0000	8.8600	118.821	2528.701	1262.626
5	140.000	6.0000	14.0100	139.024	2468.648	1314.06
6	185.000	6.0000	14.0100	124.116	2411.963	1317.523
7	140.000	12.0000	14.0100	135.080	2332.906	1392.758
8	185.000	12.0000	14.0100	120.700	2532.223	1464.129
9	124.660	9.0000	11.4350	185.943	2522.386	1751.313
10	200.340	9.0000	11.4350	130.651	2643.964	1984.127
11	162.500	3.9546	11.4350	157.903	2332.850	1792.115
12	162.500	14.0454	11.4350	142.491	2429.720	1941.748
13	162.500	9.0000	7.1044	155.618	2315.887	1422.475
14	162.500	9.0000	15.7656	127.162	2295.579	1512.859
15	162.500	9.0000	11.4350	124.425	2275.261	1344.086
16	162.500	9.0000	11.4350	124.425	2275.261	1344.086
17	162.500	9.0000	11.4350	124.425	2275.261	1344.086
18	162.500	9.0000	11.4350	124.425	2275.261	1344.086
19	162.500	9.0000	11.4350	124.425	2275.261	1344.086
20	162.500	9.0000	11.4350	124.425	2275.261	1344.086

Table 4. Linear regression models for Y_1' , Y_2' and Y_3' .

Type	Regression equations
Inverse forming rate	$Y_1' = 0.015x_1^2 + 0.534x_2^2 + 0.255x_3^2 + 0.016x_1x_2 + 0.023x_1x_3 + 0.248x_2x_3 - 5.853x_1 - 16.344x_2 - 13.461x_3 + 809.782$
Inverse tensile strength	$Y_2' = 0.22x_1^2 + 4.56x_2^2 + 2.16x_3^2 + 0.77x_1x_2 + 0.38x_2x_3 - 77.54x_1 - 209.58x_2 - 56.6x_3 + 9721.88$
Inverse elongation	$Y_3' = 0.19x_1^2 + 10.82x_2^2 - 6.6x_3^2 + 0.16x_1x_2 + 0.26x_1x_3 + 6.53x_2x_3 - 65.8x_1 - 288.17x_2 - 60.18x_3 + 7450.76$

In the equation, $\bar{b}_0, \bar{b}_i (i=1, \dots, n)$ are undetermined coefficients. To determine these coefficients, the number of experimental trials m needs to satisfy the relationship $m \geq n+1$. Let $Y^{(j)}$ be the response value obtained after m trials, and the response surface function value calculated through equation (2) is denoted as $Y^{(j)}$, then

$$\bar{Y}^{(j)} = \bar{b}_0 + \sum_{i=1}^n \bar{b}_i x_i^{(j)} \quad (3)$$

where j takes natural numbers from $\{1, \dots, m\}$, and the $\bar{Y}^{(j)}$ calculated through equation (3) is an approximate function of the response value $Y^{(j)}$. The error value ε_{es} between the two can be expressed as:

$$\varepsilon_{es} = Y^{(j)} - \bar{b}_0 - \sum_{i=1}^n \bar{b}_i x_i^{(j)}. \quad (4)$$

The above formula clarifies the form of the response surface function. However, to solve for the undetermined coefficients in the formula, the least squares principle must be used to minimize the sum of squares of ε_{es} to determine the most suitable coefficients \bar{b} in the formula. First, express formula (1) in matrix form as:

$$\bar{Y} = \bar{b}_0 + \mathbf{x}^T \mathbf{K} \mathbf{x} + \mathbf{x}^T \mathbf{L}. \quad (5)$$

In the equation, $\mathbf{x}^T = (x_1, \dots, x_k)$, $\mathbf{L}^T = (\bar{b}_1, \dots, \bar{b}_k)$, \mathbf{K} is a symmetric matrix of order k , as follows:

$$\mathbf{K} = \begin{bmatrix} \bar{b}_{11} & \dots & \bar{b}_{1k}/2 & \dots & \dots & \bar{b}_{k1}/2 & \dots & \bar{b}_{kk}/2 \end{bmatrix} \quad (6)$$

Table 5. ANOVA results of the models for Y_1 , Y_2 and Y_3 .

Source	Degrees of freedom	Sum of squares of deviation from average			Mean square			F-value			P-value		
		Y_1	Y_2	Y_3	Y_1	Y_2	Y_3	Y_1	Y_2	Y_3	Y_1	Y_2	Y_3
x_1	3	357.192	2573.6	2.351	119.06	857.87	0.784	156.52	6.24	4.228	0.000	0.001	0.001
x_2	3	61.02	418.55	0.842	20.34	139.52	0.281	27.15	1.16	0.372	0.001	0.012	0.025
x_3	3	5.147	81.32	1.695	1.716	1.24	0.565	1.68	0.21	2.302	0.0027	0.047	0.015

Table 6. ANOVA results of the models for Y_1' , Y_2' and Y_3' .

Source	Degrees of freedom	Sum of squares of deviation from average			Mean square			F-value			P-value		
		Y_1'	Y_2'	Y_3'	Y_1'	Y_2'	Y_3'	Y_1'	Y_2'	Y_3'	Y_1'	Y_2'	Y_3'
Model	9	3552.16	236929	362145	26325	26325	40238	41.27	41.27	0.68	0.000	0.000	0.0000
Linear	3	2408.83	19840	29971	62481	62481	9990	97.96	97.76	1.13	0.000	0.000	0.0000
Square	3	1091.14	195189	306245	65063	65063	102081	102.01	102.01	2.03	0.000	0.000	0.0000
Interaction	3	52.20	20875	22894	7300	6958	7631	11.45	10.92	0.22	0.001	0.025	0.0382
Residuals	8	13035.26	6843	568352	1629.41	855	71044			13.06			
Lack of fit	7	10832.71	6837	567103	1547.53	977	81015	2.87	3.24	13.06	0.206	0.627	0.561
R^2	Y_1'	85.52%		R^2_{Adj}	Y_1'	83.67%		Analog signal-to-noise ratio			Y_1'	26.45	
	Y_2'	97.38%			Y_2'	89.46%		Y_2'			Y_2'	13.02	
	Y_3'	91.27%			Y_3'	85.04%		Y_3'			Y_3'	12.61	

Derivation of equation (5) yields:

$$\bar{Y}' = -L + 2Kx. \tag{7}$$

Let equation (7) be equal to 0, the stable point x_s of the quadric surface can be solved, and substitute x_s into equation (3), the predicted response value \bar{Y}_s at the stable point can be obtained, the expression is as follows:

$$x_s = L/2K \tag{8}$$

$$\bar{Y}_s = \bar{b}_0 + 0.5x_s^T L. \tag{9}$$

Further apply the least squares algorithm to find the estimated coefficients \bar{b} in the matrix K , so that $\bar{Y} = f(x_k)$ is optimized. If the matrix $x^T x$ is non-singular, then only the following equation (5) condition needs to be satisfied by \bar{b} to obtain the mathematical model of the second-order response surface:

$$F = \sum_{j=1}^m (\epsilon_{es})^2 \rightarrow \min. \tag{10}$$

Based on the CCD experimental design results in Table 3, the second-order response surface model is fitted using the least squares method to obtain the unknown coefficients in equation (1). Subsequently, regression models for the responses Y_1' , Y_2' , and Y_3' with respect to x_1 , x_2 , and x_3 are established, as shown in Table 4.

ANOVA is a statistical model that can analyze the mean differences between multiple sets of data [24]. The test statistic F is defined as the ratio of the sum of squares between groups to the sum of squares within groups. The p -value is the density function value of the F value. The significant relationship between the optimization factors (x_1 , x_2 , and x_3) and the target variables (Y_1 , Y_2 , and Y_3), as well as regression model information, is shown in Tables 5 and 6. Generally, the smaller the p -value, the more significant the impact of the factor on the target variable. From Table 5, it can be observed that Y_1 and Y_2 have the relationship $p(x_1) < p(x_2) < p(x_3)$, while Y_3 is arranged in the order $p(x_1) < p(x_3) < p(x_2)$. Therefore, it can be inferred that x_1 and x_2 have a greater impact on Y_1 and Y_2 , while x_1 and x_3 have a greater impact on Y_3 . Additionally, from Table 6, it is noted that the p -values of the regression terms for Y_1' , Y_2' , and Y_3' are < 0.05 , indicating that the constructed response surface model rejects the null hypothesis and the regression model is overall significantly effective. The lack of fit terms for Y_1' , Y_2' , and Y_3' have p -values (> 0.05), showing that the model accepts the null hypothesis and the probability of lack of fit between predicted and observed values does not exist. The correlation coefficients R_2 ($> 85\%$) for Y_1' , Y_2' , and Y_3' are close to the adjusted coefficients, indicating a good overall fit of the model. The adjusted coefficients R_{2Adj} ($> 83\%$) for Y_1' , Y_2' , and Y_3' imply a high level of confidence in the predictive performance of the model. Furthermore, the analog signal-to-noise ratio is far greater

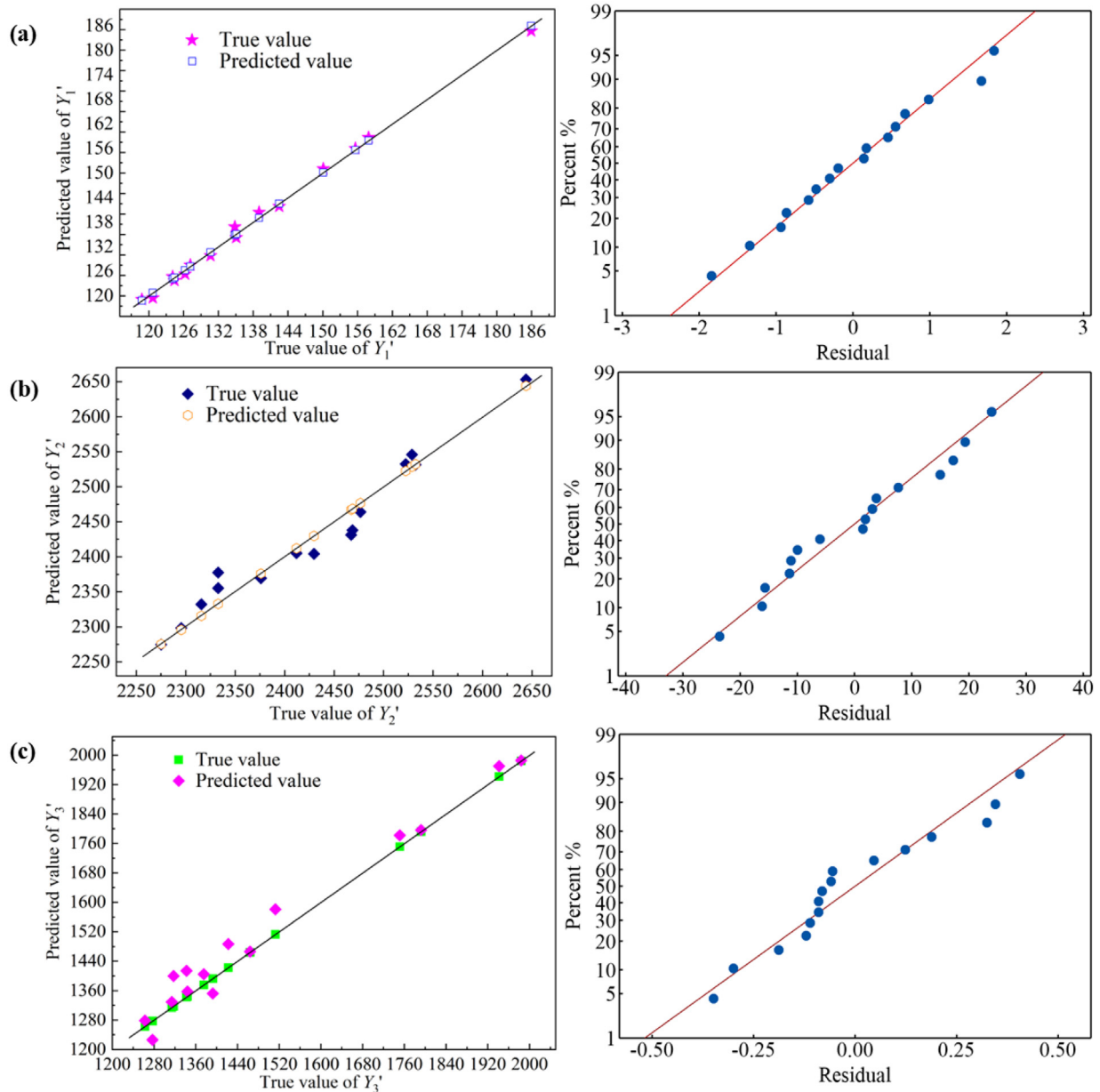


Fig. 5. Fit degrees of response surface models and residual normal probability plots for (a) Y_1' , (b) Y_2' and (c) Y_3' .

than 4, indicating that the model has sufficient discrimination power. In conclusion, the models constructed for Y_1' , Y_2' , and Y_3' exhibit high accuracy and reliability.

To further analyze the fitting effect of the model, the goodness of fit of the response surface models for Y_1' , Y_2' and Y_3' as well as the residual normal probability plots, are shown in Figure 5. From Figure 5a, 5b, and 5c, it can be observed that the predicted values of Y_1' , Y_2' and Y_3' are distributed on both sides of the 45° angle bisector line with the corresponding true values. Although there is a slight deviation from the ideal scenario where they should overlap and lie on the diagonal line, the deviation is small and can be ignored. Additionally, the residuals of Y_1' , Y_2' and Y_3' are very close to the fitted regression line, with the most dense and abundant probability density at the center of the

residuals, indicating a normal distribution of residuals and a good fit of the regression model. Therefore, this model can be used to predict the changes in the forming accuracy and mechanical properties of T-stiffened plates during the UVCAF process.

Based on the ANOVA results for Y_1 , Y_2 , and Y_3 in Table 5, it is known that x_1 and x_2 have a more significant impact on Y_1 and Y_2 , while x_1 and x_3 have a more significant impact on Y_3 . The control of the forming characteristics of the T-stiffened plates by x_3 is more complex, requiring consideration of the variations of x_1 and x_3 on Y_3 at different x_2 conditions. Therefore, to explore the interaction effects between the target variables and factors, contour plots and three-dimensional surface plots of the linear regression models for Y_1' , Y_2' , and Y_3' are shown in Figures 6–8.

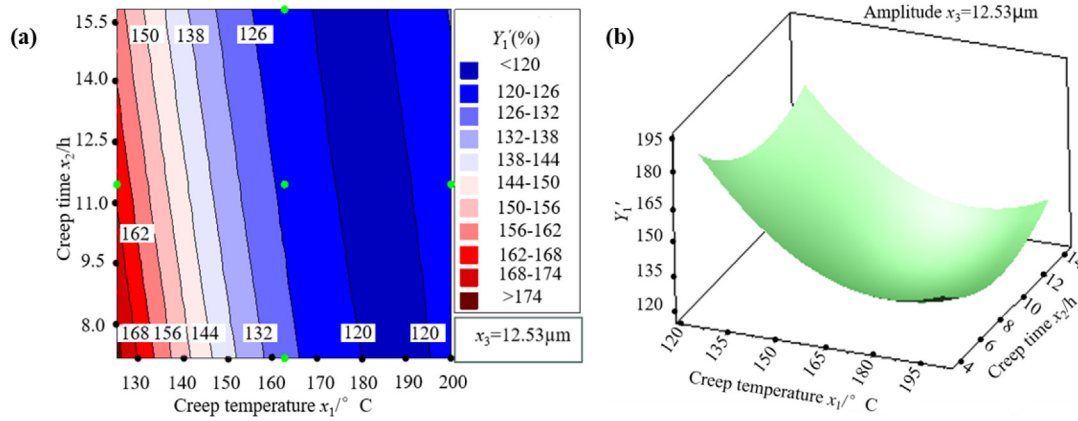


Fig. 6. (a) Contour and (b) three-dimensional surface plots for the response surface model Y_1' .

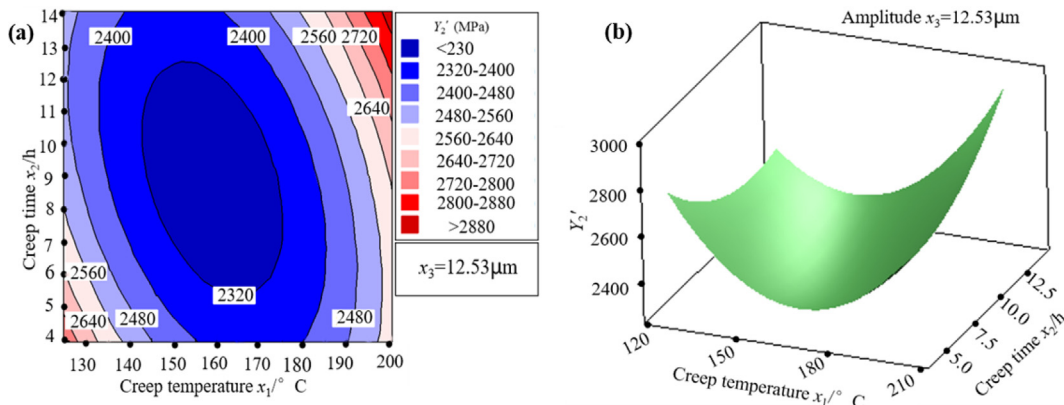


Fig. 7. (a) Contour and (b) three-dimensional surface plots for the response surface model Y_2' .

Observing Figure 6a, it is found that Y_1' decreases first and then increases with increasing x_1 , decreases with increasing x_2 , and reaches a minimum value (located in the deep blue area at 120) when the change intervals of x_1 and x_2 are [175 °C, 195 °C] and [6 h, 15 h], respectively. It can be seen that excessively high creep temperature hinders the improvement of material formability because high temperatures result in coarse material structure, reduced strength, and weakened material plasticity. In the UVCAF process, Y_1' is more significantly influenced by x_1 compared to x_2 , as shown in Figure 6b. By using Minitab to capture the optimal forming parameters corresponding to the most significant Y_1' for the T-stiffened plate [178.2 °C, 9.6 h, 13.8 μm], Y_1' is minimized to 118.71, corresponding to Y_1 at 84.25%. To obtain the confidence interval of the points on the regression model, the parameter combination [178.2 °C, 9.6 h, 13.8 μm] is substituted into the response surface model, resulting in a 95% predicted response of Y_1' at 118.85. Comparing the predicted fitted value with the corresponding optimization result shows good consistency, indicating that the regression model Y_1' is highly reliable.

From Figure 7a, it can be observed that when the amplitude $x_3 = 12.53 \mu\text{m}$, Y_2' shows a decreasing trend initially followed by an increasing trend with increasing x_1 and x_2 . When the change intervals of x_1 and x_2 are [143 °C, 175 °C] and [5.5 h, 12.5 h], respectively, Y_2' reaches a

minimum value located in the deep blue area (< 2320 MPa), while Y_2 reaches its maximum value. This is because as x_1 or x_2 increases, a large amount of strengthening phases η' and θ' precipitate within the microstructure, strengthening the alloy matrix, resulting in an increase in material tensile strength. However, when x_1 and x_2 are too large, the material undergoes over-aging, leading to a decrease in the quantity of η' or θ' phases, an increase in the size of some phases, and a decrease in density, causing Y_2 to decrease.

The interaction effects of x_1 and x_2 have a significant impact on Y_2' of the stiffened plate after UVCAF treatment, as shown in Figure 7b. Using Minitab software, it is determined that when the process parameters are [159.1 °C, 8.9 h, 12.4 μm], Y_2' is minimized and most significant at 2270.10. Substituting these values into the response surface model captures a 95% predicted response of Y_2' , with the fitted value at 2271.93. A comparison reveals a high level of consistency between the predicted fitted value and the response optimization result, effectively validating the high reliability of the regression model Y_2' . The contour plots and three-dimensional surface plots of the response surface model for Y_3' are shown in Figure 8.

When $x_2 = 6 \text{ h}$, x_1 ranges from [150 °C, 175 °C], and x_3 is less than or equal to 8 μm, the minimum value of Y_3' ranges within 1380, as shown in the contour plot in Figure 8a.

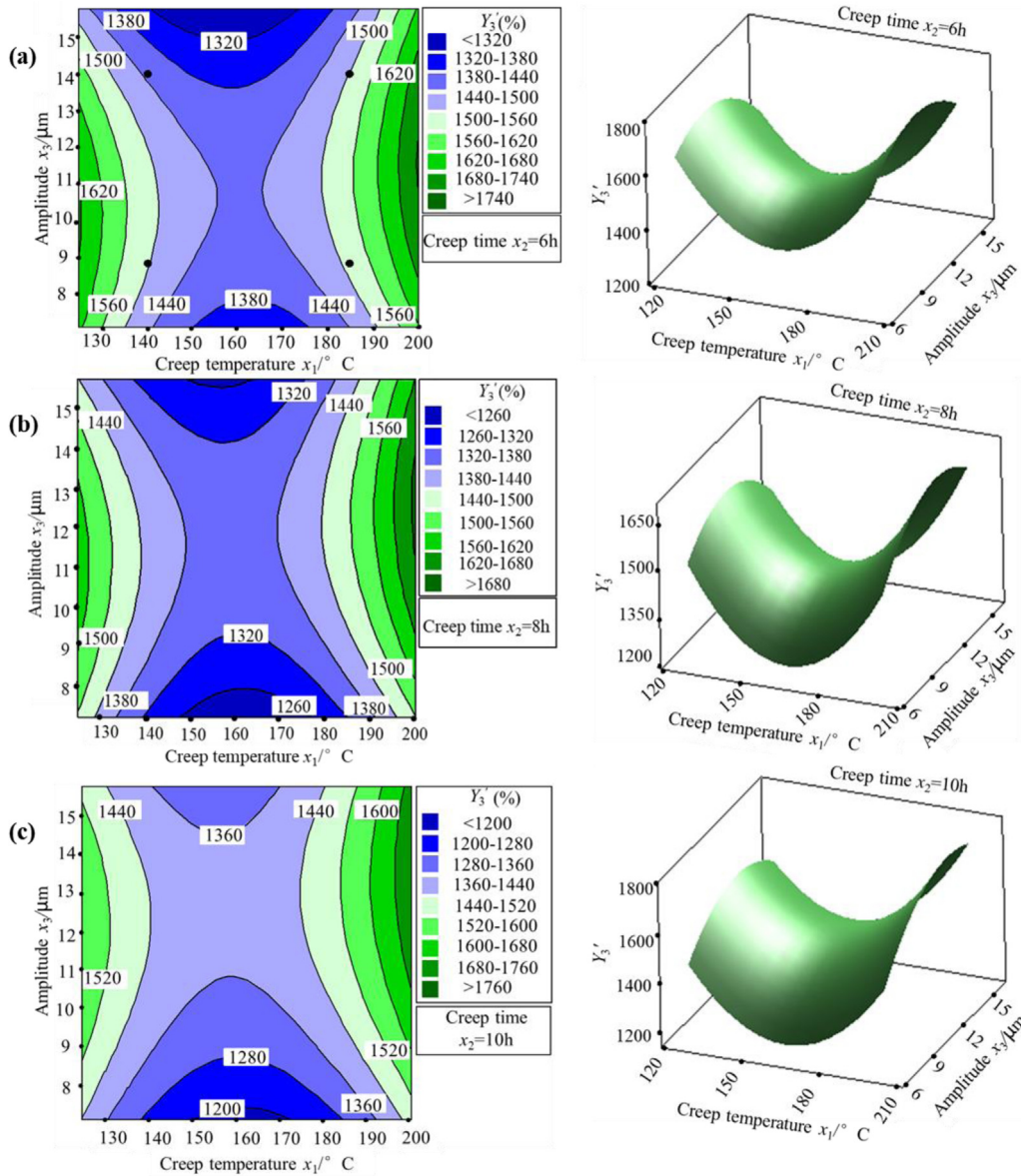


Fig. 8. Contour and three-dimensional surface plots for the response surface model Y_3' at (a) 6 h, (b) 8 h and (c) 10 h.

When $x_2 = 8$ h, x_1 ranges from [148 °C, 178 °C], and x_3 is not greater than 8 μm , the minimum value range of Y_3' is not greater than 1260, as depicted in the contour plot in Figure 8b. The contour plot in Figure 8c reveals that when $x_2 = 10$ h, x_1 ranges from [150 °C, 173 °C], and x_3 is not greater than 7.3 μm , the minimum value range of Y_3' does not exceed 1200. Furthermore, from the three-dimensional surface plots in Figures 8a, 8b, and 8c, it is evident that the effects of x_1 , x_3 , and their interaction on the Y_3' model are significant. When x_2 is 6 h, 8 h, and 10 h, Y_3' shows a decreasing trend followed by an increasing trend with increasing x_1 and x_3 , with x_1 having a more significant impact on Y_3' compared to x_3 .

Utilizing Mintab analysis tools, it is found that Y_3' reaches its minimum value at 1176.16 when $x_1 = 161.4$ °C, $x_2 = 10$ h, and $x_3 = 7.1$ μm , corresponding to Y_3 at 8.5%. To obtain the confidence interval of the points on the regression

model, the process combination [161.4 °C, 10.0 h, 7.1 μm] is input into the variables of the response surface design, capturing a 95% predicted response of the regression model Y_3' at 1187.49. The consistency between the predicted fitted value and the response optimization result validates the high reliability of the regression model Y_3' .

In summary, when x_1 ranges from [140 °C, 185 °C], x_2 ranges from [6 h, 12 h], and x_3 ranges from [8.86 μm , 14.01 μm], the R_2 values of the response surface models for Y_1' , Y_2' , and Y_3' are all greater than 85%, approaching 100%. This indicates that the above-mentioned models have a high level of accuracy and reliability globally, providing a good predictive effect on the functional relationships. The results obtained by inputting the process parameters corresponding to the response indicators into the response surface models are shown in Table 7. From Figures 6–8 and Table 7, it is observed that when each

Table 7. Results of the response surface models related to Y_1' , Y_2' and Y_3' .

$x_1(T/^\circ\text{C})$	$x_2(t/h)$	$x_3(A/\mu\text{m})$	Y_1'	Y_2'	Y_3'
178.2	9.6	13.8	118.7133	2365.816	1388.025
159.1	8.9	12.4	128.7912	2270.097	1214.113
161.4	10.0	7.1	125.83	2304.15	1176.16

response indicator is minimized, the forming process parameters are not consistent. Additionally, under the same process parameters, one response indicator may be optimal while the others are not, illustrating a typical optimization problem where multiple response indicators within a given process range interact and conflict, requiring simultaneous optimization to achieve the best results. In essence, the above method demonstrates that the established response surface models can only meet single-target optimization and cannot fulfill the requirements of multi-target optimization.

2.2.2 Multi-objective optimization via AMOGA-EWM

The essence of multi-objective optimization problems lies in the mathematical relationships formed by multiple objective functions and related equality and inequality constraints, where each objective cannot be optimized simultaneously. To obtain an effective solution set, different weights must be assigned to the objectives [25]. Since the objective functions in Table 4 are all minimization objective functions, a generic functional form with m objectives and n -dimensional design variables can be used to describe the multi-objective optimization problem of the model as follows:

$$\begin{cases} \min F(x) = [f_1(x), f_2(x), \dots, f_m(x)]^T \\ s.t. g_i(x) \leq 0, i = 1, 2, 3 \dots, p \\ h_j(x) = 0, j = 1, 2, 3 \dots, q \end{cases} \quad (11)$$

In the equation, $f_i(x) \in R^m, \{i = 1, \dots, m\}$ represents m -dimensional objective functions, $g_i(x), \{i = 1, \dots, p\}$ denotes p inequality constraint functions, $h_j(x), \{j = 1, \dots, q\}$ signifies q equality constraint functions, $x \in R_n, \{x_1, \dots, x_n\}$ represents n -dimensional design variables, and $X = \{x|x \in R^n, g_i(x) \geq 0, i = 1, \dots, p, j = 1, \dots, q\}$ defines the feasible region of equation (11).

The UVCAF process falls within the category of metal material bending processing, with a highly nonlinear and complex process involving multiple target parameters. The relationship between process parameters and the forming quality of T-stiffened plates is nonlinear, time-varying, and highly coupled, making it challenging to establish an accurate mathematical model that describes the relationship between process parameters and T-stiffened plate quality. Therefore, the essence of multi-objective optimization is to search for solutions that closely approach the Pareto optimal solution set [26].

MOGA has become a primary method for solving Pareto front solutions due to its strong pattern recognition, adaptive control, and parameter optimization advantages

[27], while EWM ensures the influence of experimental factors on the experimental indicators and the interaction between various experimental indicators [28]. AMOGA-EWM, as one of the favored algorithms for multi-objective optimization, enhances solution diversity through real number encoding and decoding, utilizes gene position mutation operators to obtain excellent individuals, and can achieve a more evenly distributed Pareto optimal solution set with strong stability and adaptability. Therefore, this study will modify the regression models in Table 4 according to equation (11), and then utilize the AMOGA-EWM algorithm to search for the multi-objective response surface models and conduct training until generating satisfactory weight values. The corresponding objective functions and constraints are as follows:

$$\begin{cases} \min Y' = (Y_1'(x), Y_2'(x), Y_3'(x)); \\ x = [x_1, x_2, x_3] \\ s.t. 140 \leq x_1 \leq 185; 6 \leq x_2 \leq 12; 8.86 \leq x_3 \leq 14.01 \end{cases} \quad (12)$$

Using the AMOGA-EWM algorithm to optimize the regression models Y_1' , Y_2' , and Y_3' , the improved minimum distance selection method is employed to capture the optimal forming process parameters from the Pareto solution set [29]. The flowchart of AMOGA-EWM is shown in Figure 9.

Firstly, input the objective functions and constraints; secondly, form new excellent individuals through crossover and mutation genetic operators; then, eliminate the poorest subpopulations, retaining the best individuals in each genetic iteration; finally, repeat the optimization process calculation according to conditions [30].

In the AMOGA-EWM algorithm, the population size (k) and the number of iterations (n) have a significant impact on obtaining the Pareto optimal solution set [31]. To enhance computational accuracy, the selection of parameters in the multi-objective optimization algorithm needs to be reasonable. In the algorithm operation, the population size is set to $k = 300$, as a larger population size increases the likelihood of finding the global solution. When iterating $n = 100$, the overall distribution is highly concentrated, indicating that $n = 100$ meets the optimization requirements. The comprehensive evaluation model for multi-objective optimization quality is derived as follows:

$$Z = f'(x) = 0.4862'Y_1 + 0.3617Y_2' + 0.1521Y_3' \quad (13)$$

Where $f'(x)$ is the reciprocal of $\bar{Y} = f(x)$, and the multi-objective optimization design results are shown in Table 8.

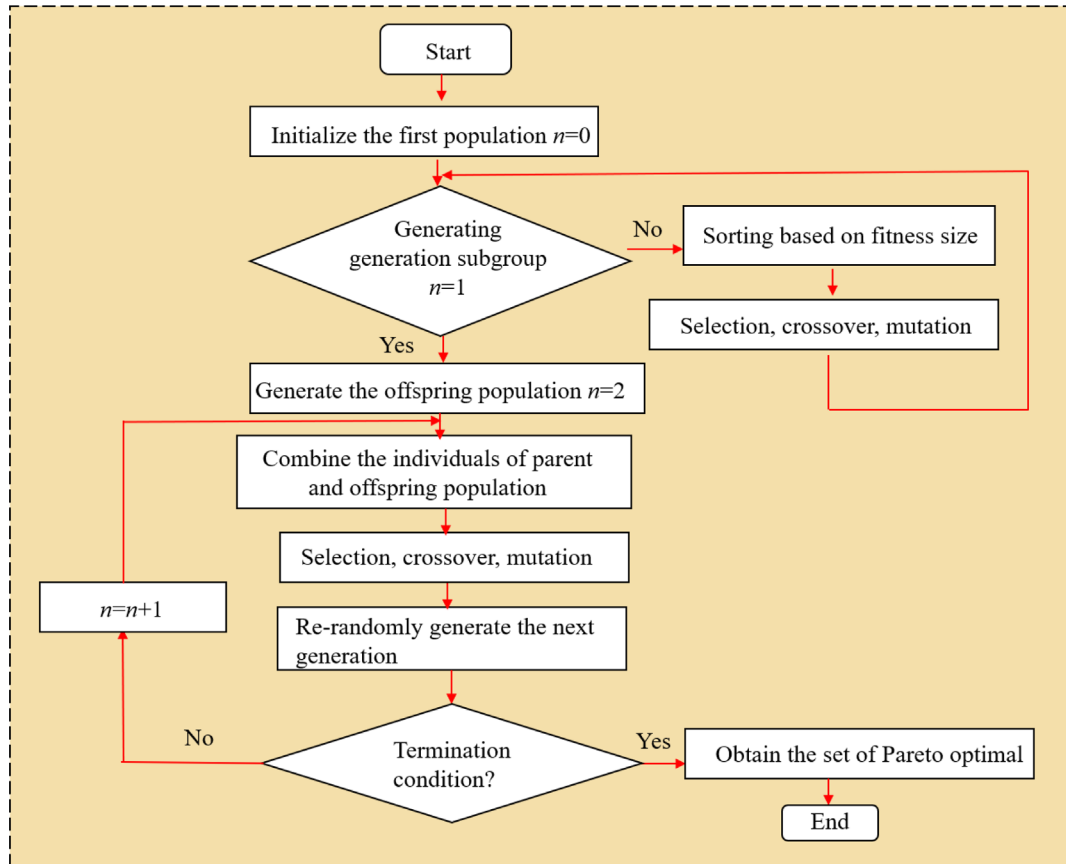


Fig. 9. The flowchart of multi-objective optimization with AMOGA-EWM algorithm.

Table 8. The optimal design results of AMOGA-EWM algorithm.

x_1 (T / °C)	x_2 (t / h)	x_3 (A / um)	Y_1'	Y_2'	Y_3'
164.8	9.2	9.6	123.65	2281.53	1367.24

2.2.3 Optimization results and confirmation tests

The optimal processing parameters mentioned above were validated in the UVCAF experiment, and the experimental results are shown in Figure 10. Upon observation of Figure 10, it is noted that the UVCAF experimental result ($Y_{1\text{exp}} = 79.6\%$) aligns well with the AMOGA-EWM computational result ($Y_{1\text{algo}} = 80.9\%$).

Further analysis reveals that the predicted results by the AMOGA-EWM algorithm (Y_1 , Y_2 , Y_3) are slightly larger by 1.3%, 1.4 MPa, and 0.2% compared to UVCAF, but they still meet engineering practical applications (5%). This indicates that capturing the optimal forming process parameters of the UVCAF experiment using the AMOGA-EWM algorithm is feasible and effective, while also demonstrating the high credibility and good predictive effect of the established response surface regression model.

2.3 Experiment design and measurement procedure

To study the effects of UVCAF and CAF under the optimal process parameters on the forming rate and mechanical properties of T-stiffened plates, the plates underwent corresponding processing and tensile tests. The process parameters under different conditions are shown in Table 9. The physical image of the T-stiffened plates after UVCAF processing is shown in Figure 11a. To accurately obtain the curvature radius after springback, a 3D scanner was used to reconstruct the three-dimensional geometric model of the T-stiffened plates, as shown in Figure 11b. Following the “Welded Joint Tensile Test Method” standard [32], the fracture conditions of the tensile specimens under different conditions are shown in Figure 11c, where #1, #2, and #3 correspond to specimens with no treatment, CAF treatment, and UVCAF treatment, respectively. The fractures of all

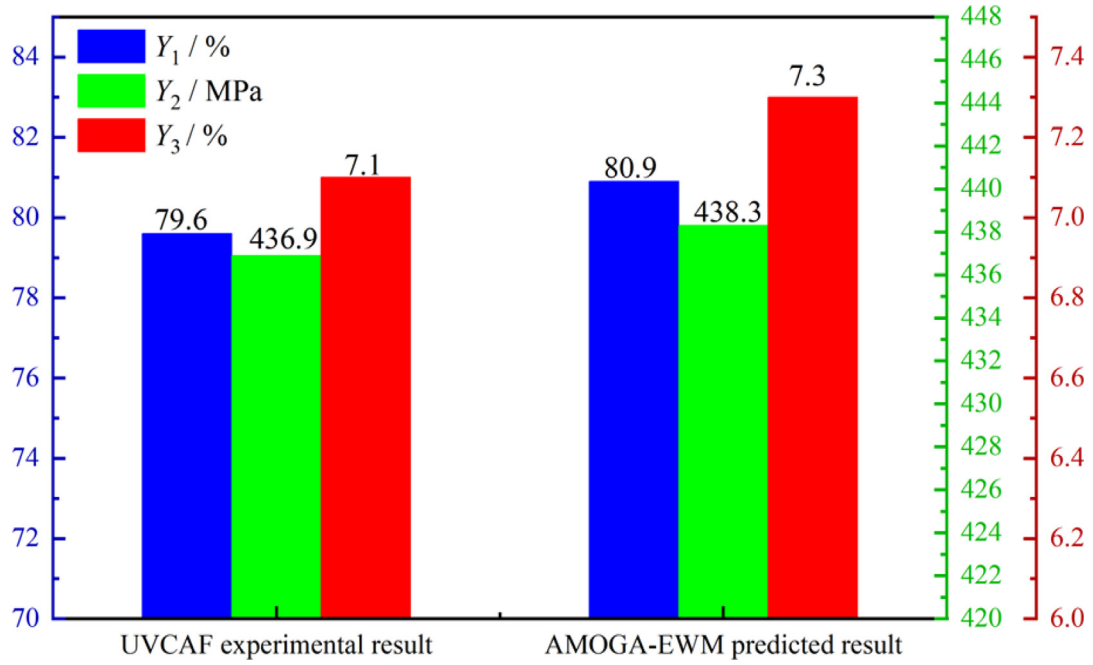


Fig. 10. Comparison of T-stiffened plate performance under UVCAF and AMOGA-EWM algorithm.

Table 9. Forming process parameters for the T-stiffened plate in different working conditions.

Working conditions	Creep temperature / °C	Creep time/h	Amplitude / μm	Creep stress/ MPa	Vibration time / s
No treatment	—	—	—	—	—
CAF	164.8	9.2	0	130	0
UVCAF	164.8	9.2	9.6	130	3600

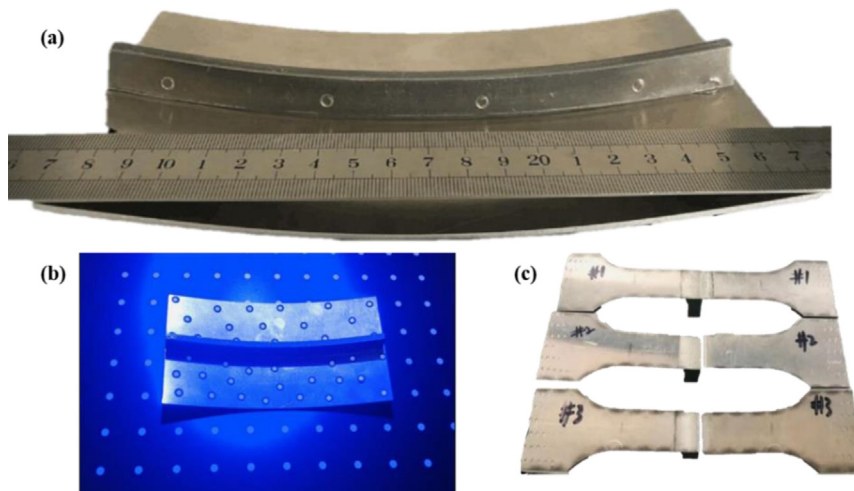


Fig. 11. Views of (a) T-stiffened plate treated by UVCAF, (b) the forming stiffened plate by 3D scanning and (c) the fracture specimens of T-joints in different working conditions.

specimens occurred in the nugget zone (NZ), and the fracture surfaces of the three samples were at a 45° angle to the direction of tension. In terms of microscopic characterization, scanning electron microscopy (SEM)

was used to observe the fracture morphology, and JEM-2000CX transmission electron microscopy (TEM) was employed to analyze the grain interior and grain boundaries of NZ in the T-stiffened plates.

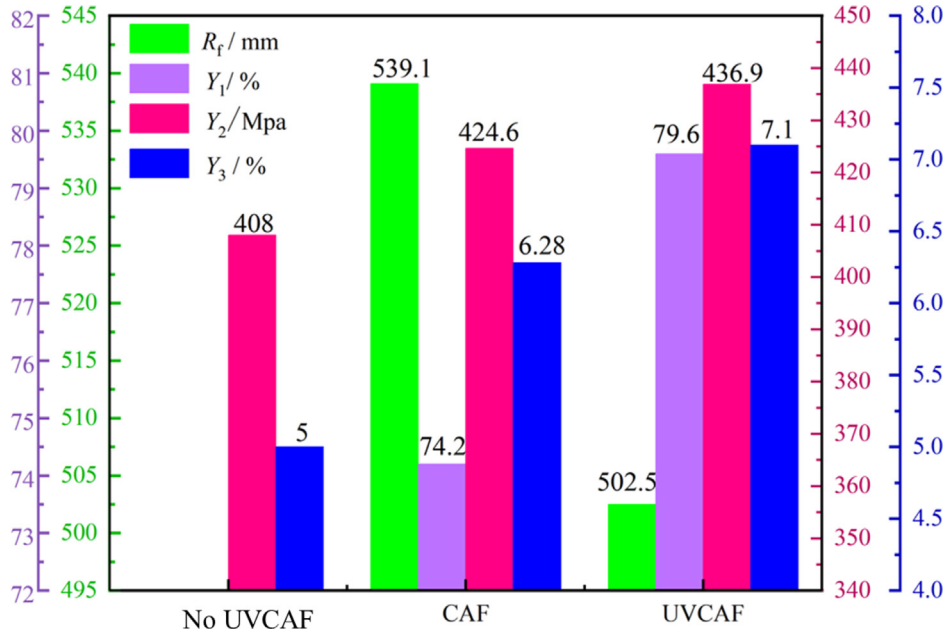


Fig. 12. Forming rates and mechanical properties of T-stiffened plate under different working conditions.

3 Experimental results and discussion

3.1 Forming rate and mechanical properties

The forming rate Y_1 and the springback rate (SP) have a complementary relationship [17]. According to equation (14), the calculation formula for Y_1 can be expressed as:

$$\begin{cases} Y_1 = 1 - SP \\ PP = 100(R_f - R_0)/R_f \end{cases} \quad (14)$$

Where $R_0 = 400$ mm. The results of the forming rate and mechanical properties obtained after testing the specimens under different conditions are shown in Figure 12. A comparison reveals that under CAF, the curvature radius of the T-stiffened plates is 539.1 mm, with Y_1 at 74.2%; while under UVCAF, the curvature radius is 502.5 mm, with Y_1 at 79.6%. Compared to the CAF experiment, the Y_1 in the UVCAF experiment increased by 5.4%, indicating a better forming effect. This is because the softening effect caused by UV reduces the steady-state creep strain rate angle, increases the steady-state creep limit, converts more elastic deformation into plastic deformation, and releases residual internal stress more thoroughly, resulting in less springback and a larger Y_1 for the T-stiffened plates.

Furthermore, it can be seen from the graph that after the UVCAF experiment, Y_2 and Y_3 are the highest, being 12.3 MPa and 0.82% larger than after the CAF experiment, respectively, and the smallest without UVCAF. This is because the stiffened plate without UVCAF treatment undergoes grain crushing under the stirring needle action, and the dynamic recrystallization caused by stirring heat makes the grains smaller and more uniform, while there is uneven stress distribution in the NZ, leading to reduced plasticity and strength [33]. In contrast, the stiffened plate after CAF treatment produces certain precipitation phases

due to creep aging, enhancing the strength and plasticity at the weld seam [34]. For the stiffened plate treated with UVCAF, the stress superposition caused by UV can soften the material, enabling more elastic deformation to transform into plastic deformation, releasing internal stress more effectively and improving plasticity. From the perspective of fracture mode, due to the combined effects of creep aging and UV, the NZ forms more numerous and smaller dimples, and more equilibrium phases are precipitated on the matrix and grain boundaries, resulting in secondary strengthening of the material [35].

In conclusion, whether it is Y_1 , Y_2 , or Y_3 , the formability control effect of UVCAF under the AMOGA-EWM algorithm is better than that of CAF. It further reveals that under the given experimental process conditions, the AMOGA-EWM optimization algorithm can achieve comprehensive optimization of Y_1 , Y_2 , and Y_3 after UVCAF, fully validating the effectiveness and feasibility of applying this method to predict composite forming processes.

3.2 Tensile fracture analysis

After the specimens from the CAF and UVCAF experiments were pulled apart, the fracture surfaces were scanned and observed to provide a deeper explanation of the quantitative relationship between the mechanical properties of the T-stiffened plates and their microstructural organization. Figure 13 shows the fracture morphology at different magnifications under SEM for different conditions.

From Figure 13a, it can be seen that the fracture surface of the specimen after the CAF experiment is mainly composed of uneven dimples, with larger pits containing fractured secondary phase particles and accompanied by multiple tearing edges, as well as the presence of varying shear steps (see Fig. 13b), indicating that the primary fracture mode of this alloy is toughness fracture caused by

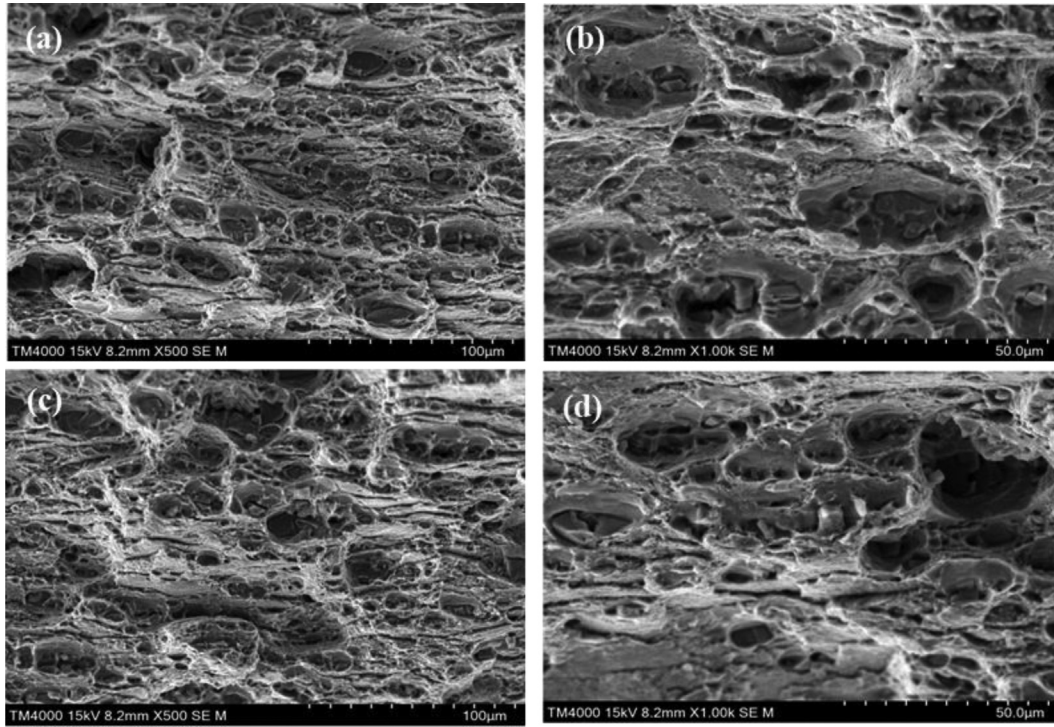


Fig. 13. Tensile fracture morphologies of (a) 500x and (b) 1000x for CAF, and (c) 500x and (d) 1000x for UVCAF.

the secondary phase. This is because the second phase distributed in the matrix has a large volume and an extremely irregular shape. Under tensile stress, deformation is relatively concentrated at the second phase, leading to a decrease in local plastic deformation capability, resulting in cracking at the second phase and matrix grain boundaries, forming microcracks that extend along the edges of the second phase grains, leading to the appearance of dimples [36]. Observing Figure 13c, it is found that with the introduction of UV, the number and depth of equiaxed dimples on the fracture surface of the specimen after the UVCAF experiment are increased. From the high-magnification electron micrograph (see Fig. 13d), it is evident that there are residual secondary phase particles at the bottom of the dimples, along with noticeable tearing edges. The increased number of tearing edges and large dimples indicates that the fracture mode of the specimen treated with UVCAF is also a toughness fracture caused by the secondary phase [35,37]. The reason may be that the softening effect generated by UV leads to an increase in the precipitation of strengthening phases in the creep aging specimen, dispersed within the matrix, acting as pinning reinforcements.

Additionally, UV enhances the accumulation of dislocation energy at the grain boundaries, leading to the formation of effective dislocation tangles that hinder dislocation slip, thereby increasing the material strength. It can be observed that the greater and more numerous the deep dimples, the more tearing edges and longer they are, and the smaller the shear step difference, the higher the strength and better the plasticity at a macro level, consistent with the changes in macroscopic tensile properties.

3.3 TEM analysis

To further investigate the microstructural changes in the NZ of the T-stiffened plates after CAF and UVCAF experiments, Figure 14 displays the bright-field microstructure of the NZ after the CAF and UVCAF experiments. The precipitation of phases within the grains significantly affects dislocation movement. The finer and more uniformly dispersed the precipitates, the stronger the hindrance to dislocation movement, leading to higher alloy strength and hardness. The release sequence of precipitates in 7055 alloy and 2197-T8 alloy is as follows: α (supersaturated solid solution) \rightarrow GP zone \rightarrow γ phase (MgZn_2) \rightarrow η phase (MgZn_2), $\alpha \rightarrow$ GP zone + δ' \rightarrow $T_1 + \delta' + \theta'$, γ phase is metastable and the main source of strengthening the aluminum base. Plate-like η phase is an equilibrium phase, and when it predominates, the alloy strength decreases [38].

As shown in Figure 14a, the alloy material after the CAF experiment contains numerous dislocations, along with a significant amount of γ phase, a small amount of η phase, and a large quantity of oblique intersecting needle-shaped precipitates of the T_1 phase. This is because creep promotes the formation of dislocations in the aluminum matrix and increases the dislocation density in the NZ through creep strain. During the creep aging process, dislocations on either side of the dislocation plane lead to stacking faults, dislocation loops, and tangled dislocations. Stacking faults provide favorable nucleation positions for the non-uniform nucleation of the T_1 phase, and the significant precipitation of T_1 leads to a reduction or even disappearance of the θ' phase. The thermal cycling during the CAF process causes the internal precipitates of the

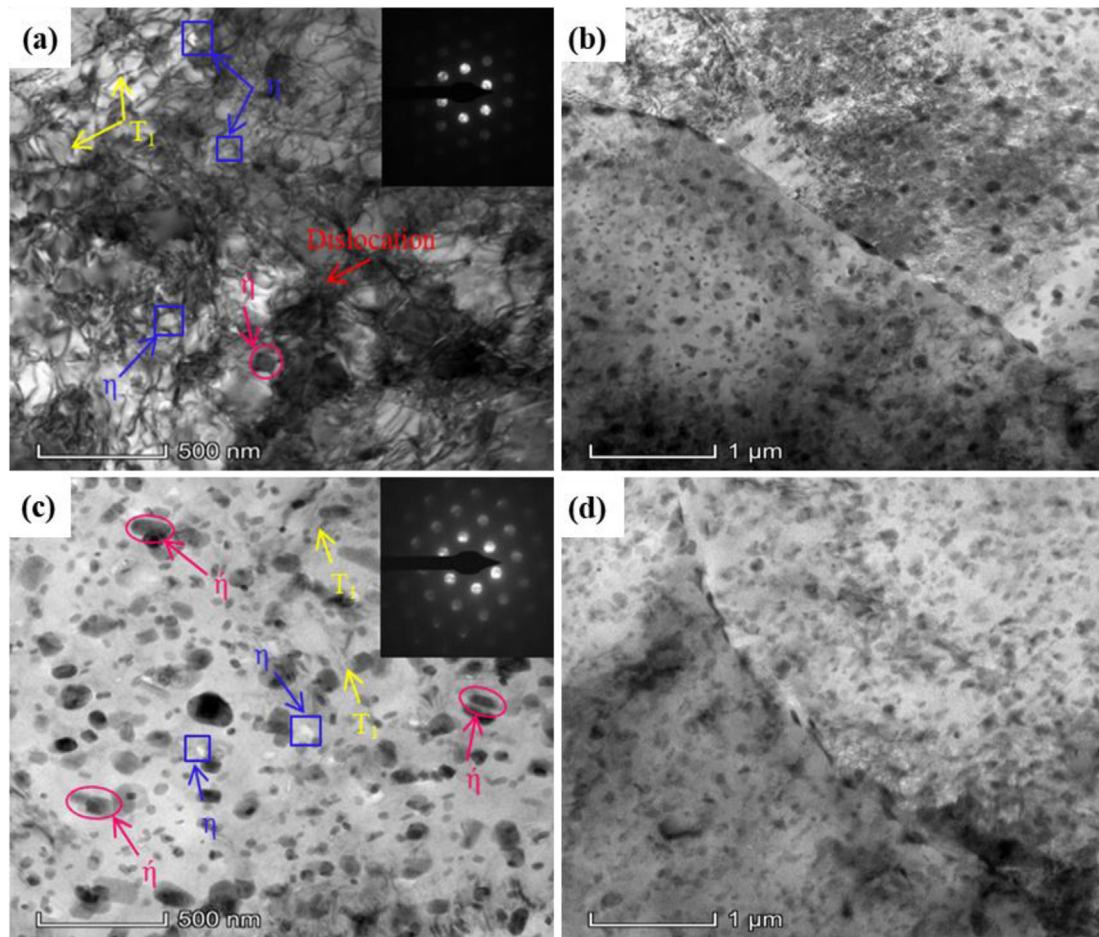


Fig. 14. TEM images of precipitation phases for (a) grain interior and (b) grain boundary under CAF, for (c) grain interior and (d) grain boundary under UVCAF.

alloy to coarsen gradually. Some metastable η' phases transform into equilibrium phases η . As seen in Figure 14b, the precipitates at the grain boundaries exist in a continuous arrangement, with smaller sizes. With prolonged thermal cycling time, the size of the η' phase at the grain boundaries decreases significantly, but there is some precipitation of the η phase with larger sizes compared to those within the grains, and the presence of a pronounced PFZ near the grain boundaries is not evident. It can be concluded that the main reinforcement of NZ comes from the combination of the T_1 phase and η' phase, leading to enhanced strength and plasticity.

Since creep promotes the formation of dislocations and stacking faults provide nucleation sites for the T_1 phase, while defects such as dislocation loops and tangled dislocations provide superior nucleation regions for the η' phase, specimens subjected to UV creep aging have a small amount of T_1 phase, a large amount of η' phase, and a small amount of equilibrium phase η within the grains, as shown in Figure 14c. Overall, the alloy is still primarily reinforced by the T_1 and η' phases, with η' phase being the most prevalent, indicating that the performance of the NZ after UVCAF is determined by the η' phase. This phenomenon is attributed to the fact that dislocations generated during creep aging are caused by vacancy damage. Excessive vacancies can

accelerate the diffusion rate of precipitates in the alloy, speeding up the precipitation behavior. Meanwhile, under the influence of creep aging, the η' phase gradually grows and coarsens. However, under the influence of UV, the η' phase is subdivided into numerous small precipitates, dispersed throughout the matrix, thereby enhancing the alloy performance. Additionally, the stress relaxation effect caused by ultrasonic softening during the creep steady-state stage can also increase the alloy strength [39].

From Figure 14d, it can be seen that with the application of UV, the precipitates at the grain boundaries become smaller, appearing in a discontinuous arrangement, and are uniformly dispersed. The larger precipitates at the grain boundaries transform from a disc shape to elongated plate-like shapes, without any significant presence of a PFZ at the grain boundaries. This is because the grain boundaries have higher dislocation energies, providing superior sites for the nucleation and growth of precipitates. The introduction of UV subdivides the grown precipitates into numerous small grains, dispersing them uniformly within the matrix, thereby improving the alloy's performance. From the above analysis, it is evident that effective UV treatment helps enhance the mechanical properties of creep-aged alloys. In contrast, alloys without UV treatment tend to produce a greater amount of large and

coarse η phases in the aluminum matrix after creep aging, leading to a decrease in alloy strength and plasticity.

4 Conclusions

This paper reports a forming method that combines ultrasonic vibration and age forming (UVCAF) aimed at achieving high quality of forming dissimilar, friction stir welded 7055-T6/2197-T8 T-stiffened plates. Firstly, a single-objective polynomial response surface model is constructed, and then the AMOGA-EWM algorithm is proposed for the multi-objective model. The optimal process plans obtained from the algorithm are used for UVCAF and CAF experiments. By means of SEM and TEM microscopic methods, the forming control effects of T-stiffened plates under different conditions are compared and analyzed. The main conclusions are as follows:

- By combining variance, fit and residual normal probability plots, it is verified that the single-objective response surface models Y_1' , Y_2' , and Y_3' constructed based on the CCD method have high accuracy and good fit. When x_1 is [140 °C, 185 °C], x_2 is [6 h, 12 h], and x_3 is [8.86 μm , 14.01 μm], the R_2 values of the three-dimensional response surface models Y_1' , Y_2' , and Y_3' are all greater than 85%, indicating that the single-objective models have good predictive performance but cannot meet the requirements of multi-objective optimization.
- The UVCAF process demonstrates strong potential for industrial application, particularly in aerospace manufacturing for large-scale, integral panel components (such as wingskins and fuselage panels) with high precision, reduced springback, and improved mechanical properties. For the UVCAF process of T-stiffened plates, an innovative multi-objective optimization quality comprehensive evaluation model based on the AMOGA-EWM algorithm is proposed. The optimal combination of process parameters is determined to be [164.8 °C, 9.2 h, 9.6 μm]. The algorithm-predicted results are only 1.3%, 1.4 MPa, and 0.2% larger than the UVCAF experimental results, demonstrating good consistency. The multi-objective optimization model established for predicting the UVCAF process of T-stiffened plates is reliable.
- The values of Y_1 , Y_2 , and Y_3 of T-stiffened plates under the UVCAF process are 5.4%, 12.3 MPa, and 0.82% larger than those under the CAF process, indicating that the softening effect produced by UV increases the steady-state creep limit of the material. This leads to more elastic deformation being converted into plastic deformation. More precisely, the specimens treated by UVCAF exhibit less springback, stronger plasticity, and better release of internal residual stresses.
- Microscopic analysis reveals that the fracture mode of specimens under both CAF and UVCAF is a ductile fracture caused by the second phase, with the fracture position located in the NZ. The main reinforcement in the NZ under CAF and UVCAF is the combination of the T_1 phase and the η phase. However, with the introduction of UV, the η phase is divided into numerous small precipitated strengthening phases, which further improves

the forming accuracy and performance of the CAF specimens.

Acknowledgments

This work was supported by Key Laboratory of Friction Welding Technologies (KLFWT), which is managed by Engineering Department in University of Tokyo, Japan. The authors are also grateful to the CAFUC's Analysis and Test Center for a test techniques and equipment.

Funding

The China Postdoctoral Science Foundation (NO.2022M722592), the Sichuan Province Engineering Technology Research Center of General Aircraft Maintenance (NO. GAMRC2023ZD03), and the Fundamental Research Funds for the Central Universities (NO.25CA-FUC04018).

Data availability statement

All data generated or analyzed during this study are included in this article.

Conflicts of interest

The authors declare that there are no conflicts of interest regarding the publication of this paper.

Author contribution statement

All authors contributed equally to this work.

Additional information

Correspondence and requests for materials should be addressed to Duquan Zuo.

References

1. T. Majeed, M.A. Wahid, M.N. Alam et al., Friction stir welding: a sustainable manufacturing process, *Mater. Today: Proc.* **46** (2021) 6558–6563
2. D. Zuo, Z. Cao, Y. Cao et al., Thermal fields in dissimilar 7055 Al and 2197 Al-Li alloy FSW T-joints: numerical simulation and experimental verification, *Int. J. Adv. Manuf. Technol.* **103** (2019) 3495–3512
3. M.C. Holman, Autoclave age forming large aluminum aircraft panels, *J. Mech. Work Technol.* **20** (1989) 477–488
4. F. Lyu, Y. Li, X. Huang et al., An investigation of creep age forming of AA7B04 stiffened plates: experiment and FE modelling, *J. Manuf. Process.* **37** (2019) 232–241
5. W. Zhou, Z. Shi, Q. Rong et al., Experimental and numerical investigations on buckling behaviour of stiffened panel during creep age forming, *Thin Wall Struct.* **172** (2022) 108940
6. F. Chen, J. Zhong, L. Zhan et al., Effect of pre-aging on creep aging properties and microstructure evolution of 2195 Al-Li alloy, *J. Mater. Res. Technol.* **21** (2022) 1029–1041

7. Y. Li, W. Zhai, Z. Cheng et al., The influence of ultrasonic vibration on parts properties during incremental sheet forming, *Adv. Manuf.* **9** (2021) 250–261
8. Z.B. Yang, Y.Q. Zhang et al., Residual stresses in ultrasonic-assisted laser sintered grinding diamond materials, *Strength Mater.* **51** (2019) 593–600
9. Z. Li, X. Li, Z. Huang et al., Ultrasonic-vibration-enhanced plasticity of an entropic alloy at room temperature, *Acta Mater.* **225** (2022) 117569
10. Y. Liu, C. Wang, R. Bi, Acoustic residual softening and microstructure evolution of T2 copper foil in ultrasonic vibration assisted micro-tension, *Mater. Sci. Eng. A* **841** (2022) 143044
11. Y. Pi, C. Gao, X. Yin, Effect of axial ultrasonic vibration on the surface topography and microstructure of Al6061 chip in extrusion cutting, *Int. J. Mater.* **17** (2024) 35–53
12. G. Han, W. Wan, Z. Zhang et al., Experimental investigation into effects of different ultrasonic vibration modes in micro-extrusion process, *J. Manuf. Process.* **67** (2021) 427–437
13. T. Zhou, C. Ma, Study of ultrasonic vibration-assisted forming in copper cylinder compression, *Procedia Manuf.* **50** (2020) 199–202
14. Y. Cao, Y. Zhu, W. Ding et al., Vibration coupling effects and machining behavior of ultrasonic vibration plate device for creep-feed grinding of Inconel 718 nickel-based superalloy, *Chinese J. Aeronaut.* **35** (2022) 332–345
15. M. Szpunar, R. Ostrowski, T. Trzepieciniski et al., Central composite design optimisation in single point incremental forming of truncated cones from commercially pure titanium grade 2 sheet metals, *Mater. (Basel, Switzerland)* **14** (2021) 3634
16. D.K. Mohanta, B. Sahoo, A.M. Mohanty, Optimization of process parameter in Al 7075 turning using grey relational, desirability function and metaheuristics, *Mater. Manuf. Process.* **38** (2023) 1615–1625
17. D. Wang, Y. Xie, Y. Guo et al., Research on process optimization and die surface compensation for high-strength steel forming springback based on Kriging model, *Forging & Stamping Technol.* **46** (2021) 62–69
18. D. Zuo, Z. Cao, Y. Cao et al., Effect of pre-stretching on microstructures and mechanical behaviors of creep-aged 7055 Al alloy and its constitutive modeling, *Metals* **9** (2019) 584
19. X. Wang, X. Guo, G. Chen et al., Remark of integral panel forming, *Modern Manuf. Technol. Equip.* (03): 1-4, 7. <https://doi.org/10.3969/j.issn.1673-5587.2008.03.001>.
20. Z. Lin, Principle and design of ultrasonic amplitude transformer, Science Press, Beijing, 1987
21. T. Zheng, L. Zhang, J. Liao, Mechanical behavior and constitutive modeling of magnesium alloy sheet in ultrasonic vibration assisted tensile test, *J. Plast. Eng.* **27** (2020) 170–176
22. S. Chen, D. Jiang, F. Ma et al., Analysis of bonding strength of metal-plastic adhesion based on central composite design, *China J. Highw. Transp.* **32** (2019) 175–182
23. P. Sagar, A. Handa, Prediction of wear resistance model for magnesium metal composite by response surface methodology using central composite design, *World J. Eng.* **18** (2021) 316–327
24. Statistics Group, Institute of Mathematics, Chinese Academy of Sciences, Analysis of variance, Science Press, Beijing, 1977
25. S. Helfrich, S. Ruzika, The weighted p-norm weight set decomposition for multiobjective discrete optimization problems, *J. Optim. Theory Appl.* **202** (2024) 1187–1216
26. Q. Zhang, J. Ding, W. Shen et al., Multiobjective particle swarm optimization for microgrids pareto optimization dispatch, *Math. Probl. Eng.* **2020** (2020) 1–13
27. W. Huang, W. Guo, P. Guo et al., Optimization design of high frequency magnetostrictive transducer based on the multi-objective genetic algorithm, *Chin. J. Sci. Instrum.* **43** (2022) 111–119
28. W. Wang, H. Li, X. Hou et al., Multi-criteria evaluation of distributed energy system based on order relation-anti-entropy weight method, *Energies* **14** (2021) 246
29. G. Sun, G. Li, G. Zheng et al., Multi-objective optimization for sheet metal forming of drawing with successive response surface method, *Chin. J. Theor. Appl. Mech.* **42** (2010) 245–255
30. J. Li, W. Zuo, E. Jiaqiang et al., Multi-objective optimization of mini U-channel cold plate with SiO₂ nanofluid by RSM and NSGA-II, *Energy* **242** (2022) 123039
31. Q. Wan, X. Jia, Multi-objective optimization of CFRP drilling parameters with a hybrid method integrating the ANN, NSGA-II and fuzzy C-means, *Compos. Struct.* **235** (2020) 111803
32. General Administration of Quality Supervision, Inspection and Quarantine of the People's Republic of China, Standardization Administration of China. GB/T 2651 — 2008, Tensile test method of welded joints, Standards Press of China, Beijing, 2008
33. D. Jacquin, G. Guillemot, A review of microstructural changes occurring during FSW in aluminium alloys and their modelling, *J. Mater. Process. Technol.* **288** (2021) 116706
34. J. Tang, B. Yu, J. Zhang et al., Effects of pre-deformation mode and strain on creep aging bend-forming process of Al-Cu-Li alloy, *T Nonfer. Metal. Soc.* **30** (2020) 1227–1237
35. D. Liu, J. Chen, B. Li et al., Effect of ultrasonic vibration-assisted two-stage age forming on properties of 7075 aluminum alloy, *Int. J. Adv. Manuf. Technol.* **115** (2021) 3485–3492
36. F. Tioguem, F. N'guyen, M. Maziere et al., Advanced quantification of the carbide spacing and correlation with dimple size in a high-strength medium carbon martensitic steel, *Mater. Charact.* **167** (2020) 110531
37. Z. Zhou, Q. Wang et al., Ultra-fine Nbss/Nb5Si3 in situ composites with remarkable properties prepared by ultrasonic melt treatment, *J. Alloy Compd.* **940** (2023) 168940
38. J. Zuo, L. Hou, J. Shi et al., Effect of deformation induced precipitation on grain refinement and improvement of mechanical properties AA 7055 aluminum alloy, *Mater. Charact.* **130** (2017) 123–134
39. M. Zohrevand, M. Aghaie-Khafri, F. Forouzan et al., Microstructural evolutions under ultrasonic treatment in 304 and 316 austenitic stainless steels: impact of stacking fault energy, *Steel Res. Int.* **92** (2021) 2100041

Cite this article as: Duquan Zuo, Yanjie Han, Ti Ye, Tianyu Xu, Shilin Feng, Yuanxiu Zhang, Shaoqing Jin, Sean Gao, Multi-objective optimization of the process combining ultrasonic vibration and age-forming of dissimilar friction-stir-welded Aluminium T-stiffened plates, *Manufacturing Rev.* **13**, 1 (2026), <https://doi.org/10.1051/mfreview/2025028>